Journal of Statistical Physics, Vol. 95, Nos. 5/6, 1999

Monte Carlo Simulations for Spinodal Decomposition

Evelyn Sander[1] **and Thomas Wanner**[2]

Received July 22, 1998; final November 30, 1998

This paper addresses the phenomenon of spinodal decomposition for the Cahn–Hilliard equation. Namely, we are interested in why most solutions to the Cahn–Hilliard equation which start near a homogeneous equilibrium $u_0 \equiv \mu$ in the spinodal interval exhibit phase separation with a characteristic wavelength when exiting a ball of radius R in a Hilbert space centered at u_0. There are two mathematical explanations for spinodal decomposition, due to Grant and to Maier-Paape and Wanner. In this paper, we numerically compare these two mathematical approaches. In fact, we are able to synthesize the understanding we gain from our numerics with the approach of Maier-Paape and Wanner, leading to a better understanding of the underlying mechanism for this behavior. With this new approach, we can explain spinodal decomposition for a longer time and larger radius than either of the previous two approaches. A rigorous mathematical explanation is contained in a separate paper. Our approach is to use Monte Carlo simulations to examine the dependence of R, the radius to which spinodal decomposition occurs, as a function of the parameter ε of the governing equation. We give a description of the dominating regions on the surface of the ball by estimating certain densities of the distributions of the exit points. We observe, and can show rigorously, that the behavior of most solutions originating near the equilibrium is determined completely by the linearization for an unexpectedly long time. We explain the mechanism for this unexpectedly linear behavior, and show that for some exceptional solutions this cannot be observed. We also describe the dynamics of these exceptional solutions.

KEY WORDS: Cahn–Hilliard equation; spinodal decomposition; phase separation; exit distributions; density estimation; Monte Carlo method; Galerkin approximation.

Dedicated to John W. Cahn on the occasion of his 70th birthday.

[1] Department of Mathematical Sciences, George Mason University, Fairfax, Virginia 22030; e-mail: sander@math.gmu.edu.

[2] Department of Mathematics and Statistics, University of Maryland, Baltimore County, Baltimore, Maryland 21250; e-mail: wanner@math.umbc.edu.

1. INTRODUCTION

The Cahn–Hilliard equation has proved to be an excellent model for several physical phenomena occurring in binary alloys. One particularly intriguing phenomenon is *spinodal decomposition*:[5, 16, 19] If a homogeneous high-temperature mixture of two metallic components is rapidly quenched to a certain lower temperature, then a sudden phase separation sets in. The mixture quickly becomes inhomogeneous and forms a fine-grained structure, more or less alternating between the two alloy components.

In order to describe this phase separation process (as well as other phenomena) Cahn and Hilliard[3, 6] proposed the fourth-order parabolic partial differential equation

$$\begin{aligned} u_t &= -\Delta(\varepsilon^2 \Delta u + f(u)) \qquad \text{in } \Omega \\ \frac{\partial u}{\partial \nu} &= \frac{\partial \Delta u}{\partial \nu} = 0 \qquad \text{on } \partial\Omega. \end{aligned} \tag{1}$$

Here $\Omega \subset \mathbb{R}^n$ is a bounded domain in $\mathbb{R}^n$ with sufficiently smooth boundary, $n \in \{1, 2, 3\}$, and the function $-f$ is the derivative of a double-well potential F, the standard example being the cubic function $f(u) = u - u^3$ with double-well potential $F(u) = (u^2 - 1)^2/4$. Furthermore, ε is a small positive parameter modeling interaction length. In this formulation, the variable u represents the concentration of one of the two components of the alloy, subject to an affine transformation such that the concentrations 0 or 1 correspond to u being -1 or 1, respectively. The Cahn–Hilliard equation is *mass-conserving*, i.e., the total concentration $\int_\Omega u\, dx$ remains constant along any solution u. Moreover, (1) is an $H^{-1}(\Omega)$-*gradient system* with respect to the van der Waals free energy functional

$$E_\varepsilon[u] := \int_\Omega \left(\frac{\varepsilon^2}{2} \cdot |\nabla u|^2 + F(u) \right) dx \tag{2}$$

where F is the primitive of $-f$ as mentioned above. [See Fife.[13]]

Every constant function $u_0 \equiv \mu$ is a stationary solution of (1). Furthermore, this equilibrium is unstable if μ is contained in the *spinodal interval*. This is the (usually connected) set of all $\mu \in \mathbb{R}$ such that $f'(\mu) > 0$. Thus, if μ lies in the spinodal interval, any orbit originating near u_0 is likely to be driven away—and explaining precisely how this happens lies at the heart of explaining the phenomenon of spinodal decomposition.

There have been many works in the physics literature dealing with spinodal decomposition and how it is modeled by the Cahn–Hilliard equa-

tion. We refer the reader to Cahn,[4,5] Hilliard,[16] Langer,[19] Elder, Desai,[9] Elder, Rogers, Desai,[10] and Hyde *et al.*,[18] just to name a few. Also, there exist numerous papers on numerical simulations of the Cahn–Hilliard equation, see for example Elliott, French,[12] Elliott,[11] Copetti, Elliott,[8] Copetti,[7] and Bai *et al.*[1,2]

Mathematical treatments of spinodal decomposition in the Cahn–Hilliard equation have appeared only recently. See Grant,[14] Maier-Paape and Wanner.[20,21] Since spinodal decomposition is concerned with solutions of (1) originating near the homogeneous equilibrium $u_0 \equiv \mu$, it is not surprising that both of the above approaches crucially rely on the properties of the linearization of (1) at u_0, i.e., the linear equation

$$\begin{aligned} v_t = A_\varepsilon v := -\Delta(\varepsilon^2 \Delta v + f'(\mu)\, v) \qquad & \text{in } \Omega \\ \frac{\partial v}{\partial \nu} = \frac{\partial \Delta v}{\partial \nu} = 0 \qquad & \text{on } \partial\Omega. \end{aligned} \tag{3}$$

We consider this linearization applied to the affine subspace of functions, with fixed mass, which obey the equation boundary conditions. More precisely, define

$$X := \left\{ v \in L^2(\Omega) : \int_\Omega v \, dx = 0 \right\} \tag{4}$$

and

$$D(A_\varepsilon) := \{ v \in X \cap H^4(\Omega) : \partial v/\partial \nu(x) = \partial \Delta v/\partial \nu(x) = 0,\ x \in \partial\Omega \} \tag{5}$$

where $H^4(\Omega) \subset L^2(\Omega)$ denotes the space of functions with four weak derivatives in $L^2(\Omega)$. It is possible to show that with this domain, the linear operator A_ε is self-adjoint. The spectrum of A_ε consists of real eigenvalues $\lambda_{1,\varepsilon} \geqslant \lambda_{2,\varepsilon} \geqslant \cdots \to -\infty$ with corresponding eigenfunctions $\varphi_{1,\varepsilon}, \varphi_{2,\varepsilon}, \ldots$. To further describe these eigenvalues, let $0 < \kappa_1 \leqslant \kappa_2 \leqslant \cdots \to +\infty$ and $\psi_1, \psi_2, \ldots$ denote the eigenvalues and eigenfunctions of the operator $-\Delta: X \to X$ subject to Neumann boundary conditions. Then the eigenvalues $\lambda_{i,\varepsilon}$ of A_ε are obtained by ordering the numbers

$$\tilde{\lambda}_{i,\varepsilon} := \kappa_i (f'(\mu) - \varepsilon^2 \kappa_i), \qquad i \in \mathbb{N} \tag{5}$$

See Fig. 1. The eigenfunctions $\varphi_{i,\varepsilon}$ are obtained from the eigenfunctions ψ_i through this ordering process in the obvious way, and form a complete

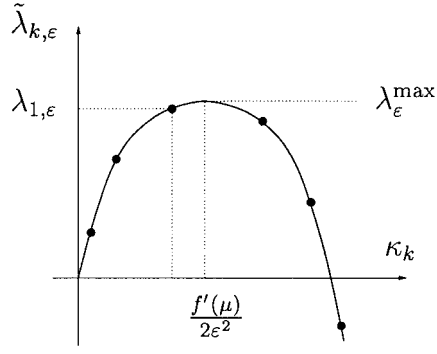

Fig. 1. Eigenvalues of the linearization A_ε.

$L^2(\Omega)$-orthogonal set in X. Moreover, the largest eigenvalue $\lambda_{1,\varepsilon}$ is of the order

$$\lambda_{1,\varepsilon} \sim \lambda_\varepsilon^{\max} := \frac{f'(\mu)^2}{4\varepsilon^2}, \qquad \text{and} \qquad \lambda_{1,\varepsilon} \leqslant \lambda_\varepsilon^{\max}, \tag{6}$$

as in Maier-Paape, Wanner[20] and Fig. 1. The strongest unstable directions are the ones corresponding to $\kappa_k \approx f'(\mu)/(2\varepsilon^2)$, and one would expect that most solutions of (3) originating near 0 will be driven away in some of these unstable directions.

In order to deduce results about the dynamics of the nonlinear Cahn–Hilliard equation from the above linearization, Grant[14] and Maier-Paape, Wanner[20,21] employed a dynamical approach. It is known that (1) generates a nonlinear semiflow $T_\varepsilon(t)$, $t \geqslant 0$, on the affine space $\mu + X^{1/2}$, where $X^{1/2}$ denotes the Hilbert space

$$X^{1/2} := \{ v \in H^2(\Omega) \cap X : \partial v/\partial \nu = 0 \text{ on } \partial\Omega \} \tag{7}$$

$H^2(\Omega) \subset L^2(\Omega)$ is the Hilbert space of functions with two weak derivatives in $L^2(\Omega)$. The constant function $u_0 \equiv \mu$ is an equilibrium point for T_ε, and the linearization of T_ε at u_0 is given by the analytic semigroup S_ε generated by A_ε.

Using the above setting, Grant[14] described spinodal decomposition for one-dimensional domains Ω. Fig. 2 gives an example of an orbit exhibiting spinodal decomposition. Roughly speaking, Grant showed that for generic small ε most solutions of (1) starting in a sufficiently small neighborhood U_ε of $u_0 \equiv \mu$ closely follow a strongly unstable one-dimensional manifold for a long time. This unstable manifold is tangent to the eigenfunction $\varphi_{1,\varepsilon}$

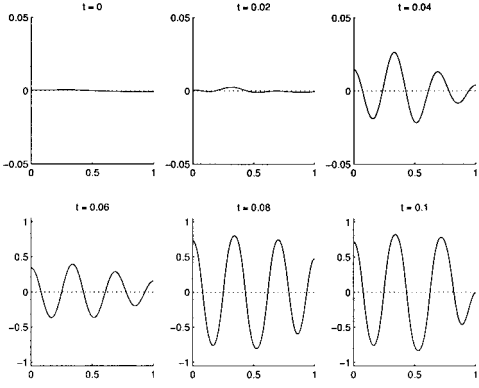

Fig. 2. Spinodal decomposition in one space dimension, $\varepsilon = 0.04$.

of the largest eigenvalue $\lambda_{1,\varepsilon}$, which is simple for generic values of ε. Grant also proved that the two branches of the strongly unstable manifold converge to periodic equilibrium points of (1), whose period is proportional to ε as $\varepsilon \to 0$ and whose L^∞-norm is bounded away from 0. Thus, these equilibria can be interpreted as spinodally decomposed states. Over time, most solutions originating in U_ε grow near the spinodally decomposed states. Thus these orbits exhibit spinodal decomposition.

Unfortunately, for higher-dimensional domains Grant's approach predicts evolution of most orbits towards regular patterns which are not observed in practice. Maier-Paape and Wanner[20, 21] pointed out that this discrepancy is due to the fact that the size of the neighborhood U_ε in Grant's result is of the order $\exp(-c/\varepsilon)$. Since ε models interaction length, an effect which occurs on the atomic level, it is extremely small. The actual size of ε depends on the specific materials. To achieve material independent results, one considers the asymptotic behavior as $\varepsilon \to 0$. Thus, the behavior of solutions described by Grant cannot be observed in the physical system. To address this, Maier-Paape and Wanner proposed a different approach for explaining spinodal decomposition, which applies to higher-dimensional domains Ω as well. They also consider solutions of (1) starting in a small neighborhood U_ε of the homogeneous equilibrium $u_0 \equiv \mu$. This time however, the size of U_ε is proportional to $\varepsilon^{\dim \Omega}$. It is proved in refs. 20 and 21 that most solutions of (1) originating in U_ε exit a larger neighborhood $V_\varepsilon \supset U_\varepsilon$ close to a dominating linear subspace $\mathscr{Y}_\varepsilon$. This subspace is spanned by the eigenfunctions corresponding to a small percentage of the largest eigenvalues of A_ε, hence its dimension is proportional to $\varepsilon^{-\dim \Omega}$. Furthermore, the functions in $\mathscr{Y}_\varepsilon$ exhibit exactly the spinodally decomposed patterns that can be observed in experiments.

Yet, although the approach by Maier-Paape and Wanner predicts the correct patterns observed in spinodal decomposition, their result is still not optimal. The size of the neighborhood V_ε is of the same order as the size of U_ε, namely proportional to $\varepsilon^{\dim \Omega} \ll 1$. In practice however, the patterns they predict are observed until the maximum norm of the solution is of order 1.

In this paper we use extensive numerical simulations to investigate the range of validity of the above two approaches—leading to a surprising observation. It turns out that most solutions of (1) stay close to the solutions of the linearized equation with the same initial conditions for considerably larger neighborhoods V_ε than the ones obtained in ref. 21. In fact, it remains valid for sizes for which one would normally expect fully nonlinear behavior of (1). Moreover, we are able to identify and describe the delicate mechanism which is responsible for this exceptional behavior. Spinodal decomposition is a result of the fact that with high probability, solutions of (1) originating near $u_0 \equiv \mu$ are pushed into a region of phase space in which the behavior of the Cahn–Hilliard equation is essentially linear. Linear behavior persists until the maximum norm of the solution reaches a certain threshold radius, independent of ε. More precisely, we state the following conjecture for the one-dimensional Cahn–Hilliard equation.

Conjecture 1.1 (Unexpectedly linear behavior). Consider solutions u and v of (1) and (3), respectively, starting at the same initial condition in a ball of radius r in $\mu + X^{1/2}$ around $u_0 \equiv \mu$. Pick a small constant d. Then with high probability, the relative difference $\|u-v\|_{H^2(\Omega)}/\|v\|_{H^2(\Omega)}$ between the linear and nonlinear solutions is less than d up to norm $\|u\|_{H^2(\Omega)} \approx C \cdot \varepsilon^{-2}$, where C is independent of ε.

For a partial proof of this conjecture (for one, two, and three space dimensions), we refer the reader to Sander, Wanner.[22] This conjecture is stated for the mathematically natural $H^2(\Omega)$-norm, rather than the physical $L^\infty(\Omega)$-norm. Our numerical simulations indicate that the relative distance between the linear and nonlinear solutions stays small up to order one with respect to ε in the $L^\infty(\Omega)$-norm. For further results relating these two norms, see ref. 21.

This paper is organized as follows. In Section 2 we use Monte Carlo simulations for one-dimensional domains Ω to obtain a precise picture of where most solutions starting in U_ε exit V_ε. This is done for balls V_ε of different sizes. It shows that for most solutions originating in U_ε, the range of validity of the linear regime is much larger than one would expect. In addition, we conclude that even in one space dimension, the dimension of the

exit set from V_ε grows as $\varepsilon \to 0$. The numerical method and basic setting for our simulations is described in Subsection 2.1. In the following two subsections, we describe regions on the exit balls in terms of the Fourier coefficients of the solutions at the time of exit. In Subsection 2.2, the mean value and standard deviation of the Fourier coefficients are shown for various exit balls and ε values. Subsection 2.3 contains estimates for the corresponding density functions.

Further investigations of the unexpectedly linear behavior are contained in Section 3. In Subsection 3.1, we numerically determine the size of the maximal ball V_ε for which the behavior of most solutions originating in U_ε is linear. We also describe the mechanism responsible for this. Subsection 3.2 shows that the previous results are of a probabilistic rather than deterministic nature, i.e., there are solutions which do not exhibit the above kind of linear behavior. We describe the dynamics of these exceptional solutions. Some concluding remarks are contained in Section 4.

2. THE MONTE CARLO SIMULATIONS

2.1. Basic Setup

In order to compare and test the validity of the approaches to spinodal decomposition by Grant[14] and Maier-Paape, Wanner[20,21] we perform the following Monte Carlo simulation. Fix the parameter ε in the Cahn–Hilliard equation, fix an initial total mass μ in the spinodal interval, as well as two radii $0 < r < R$. Now randomly choose an initial condition u_s in the ball $U_\varepsilon := B_r(u_0)$ of radius r (with respect to the $H^2(\Omega)$-norm) around the homogeneous equilibrium $u_0 \equiv \mu$. Follow the solution of the Cahn–Hilliard equation (1) starting in u_s until it exits the ball $V_\varepsilon := B_R(u_0)$ at a *first exit point* u_e. This procedure defines a map

$$\mathscr{E}_R(u_s) := u_e \in \partial V_\varepsilon \tag{8}$$

on a suitable subset of U_ε; namely the set of all initial conditions leading to orbits which leave V_ε.

Now choose the initial conditions u_s uniformly in U_ε, in a way which we make precise later. Then the above-defined map $\mathscr{E}_R$ defines an *exit distribution* on the boundary of V_ε, which contains all the information about the preferred exit region from V_ε. We now describe this measure on the infinite-dimensional set ∂V_ε.

As we point out in the introduction, the natural phase space of the abstract evolution equation associated with (1) is the affine space $\mu + X^{1/2}$. For the sake of simplicity, let us assume from now on that $\mu = 0$. The

general case can be reduced to this special situation via a suitable variable transformation, see Maier-Paape, Wanner.[21] Furthermore, let us consider the norm $\|\cdot\|_*$ on the Hilbert space $X^{1/2}$ defined by

$$\|u\|_* := (\|u\|^2_{L^2(\Omega)} + \|\Delta u\|^2_{L^2(\Omega)})^{1/2}$$

and let ψ_k, $k \in \mathbb{N}$, denote the eigenfunctions of $-\Delta$ defined in the introduction. If we set

$$\tilde{\varphi}_k := \frac{1}{\sqrt{1+\kappa_k^2}} \cdot \psi_k, \qquad k \in \mathbb{N} \tag{9}$$

then $\tilde{\varphi}_k$ is the eigenfunction of A_ε corresponding to the eigenvalue $\tilde{\lambda}_{k,\varepsilon}$, cf. (5). Moreover, the set $\tilde{\varphi}_k$, $k \in \mathbb{N}$, is a complete orthonormal set in $X^{1/2}$ with respect to the scalar product $(\cdot,\cdot)_*$ induced by $\|\cdot\|_*$.

According to Maier-Paape, Wanner[20,21] the exit distribution defined above is concentrated near a dominating subspace, which is generated by a suitable subset of these eigenfunctions. Therefore, it seems reasonable to describe the functions in $X^{1/2}$ in terms of their Fourier coefficients with respect to the eigenfunctions $\tilde{\varphi}_k$, where $k \in \mathbb{N}$. Figure 3 shows the evolution of the Fourier modes of the orbit in Fig. 2. (In these diagrams, the kth Fourier coefficient is plotted as a function of k using a polygonal path.) For any $u_s \in U_\varepsilon$ such that $\mathscr{E}_R(u_s)$ is defined as in (8), let $c_{k,R}(u_s) \in \mathbb{R}$ denote its kth Fourier coefficient, i.e., let

$$c_{k,R}(u_s) := (\mathscr{E}_R(u_s), \tilde{\varphi}_k)_* \tag{10}$$

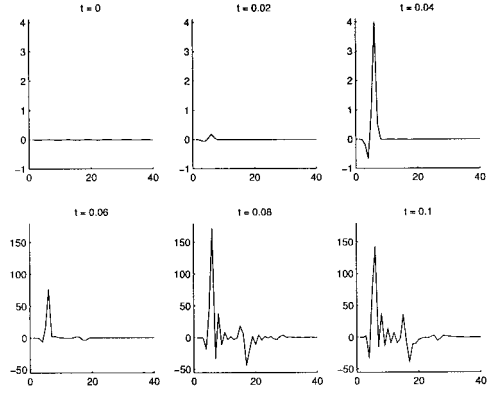

Fig. 3. Evolution of the Fourier modes for the orbit depicted in Fig. 2, $\varepsilon = 0.04$.

Then

$$\mathscr{E}_R(u_s) = \sum_{k=1}^{\infty} c_{k,R}(u_s)\, \tilde{\varphi}_k$$

and we obtain an equivalent description of the exit points in terms of real sequences.

Thus, choosing the initial conditions u_s uniformly in U_ε induces an exit distribution on the set of sequences, as well as *one-dimensional* exit distributions for the Fourier modes $c_{k,R}$, $k \in \mathbb{N}$. These one-dimensional distributions can be used to analyze the approaches due to Grant and Maier-Paape, Wanner. For example, the results by Maier-Paape and Wanner[20, 21] imply that as long as r and R are proportional to $\varepsilon^{\dim \Omega}$, the distribution of the kth Fourier mode $c_{k,R}$ is concentrated at 0, unless the corresponding eigenvalue $\tilde{\lambda}_{k,\varepsilon}$ is close to $\lambda_\varepsilon^{\max}$. Likewise, for one-dimensional domains Ω, Grant's result predicts that for odd f and $\mu = 0$ the distribution of $c_{k,R}$ is concentrated at two points $\pm\gamma_k$, where γ_k, $k \in \mathbb{N}$, denote the Fourier coefficients of the intersection point of V_ε with the one-dimensional strongly unstable manifold at u_0. In fact, our simulations show that a third point of view is more appropriate. Namely, it turns out that the correct way to think of dominating modes versus non-dominating modes is with respect to the linearized behavior—even though we consider a nonlinear equation.

For $\Omega = (0, 1)$ we present detailed information on the distributions of the Fourier modes $c_{k,R}$ in the following two subsections. This is achieved numerically by employing a Monte Carlo simulation, where we use randomly chosen initial conditions near the equilibrium. Similar to Bai *et al.*[2, 1] we approximate the one-dimensional Cahn–Hilliard equation (1) with a standard Galerkin spectral method. For sufficiently large integers N we seek approximations $u_N(t)$ to the solutions of the Cahn–Hilliard equation in the finite-dimensional space

$$X_N := \operatorname{span}\{\tilde{\varphi}_1, \ldots, \tilde{\varphi}_N\}$$

i.e., which are of the form

$$u_N = \sum_{k=1}^{N} a_k \tilde{\varphi}_k, \qquad a_k \in \mathbb{R} \tag{11}$$

Note that for $\Omega = (0, 1)$ we have $\kappa_k = k^2\pi^2$ and $\psi_k(x) = \sqrt{2} \cdot \cos k\pi x$, so that

$$\tilde{\varphi}_k(x) = \frac{\sqrt{2}}{\sqrt{1 + k^4\pi^4}} \cdot \cos k\pi x, \qquad \text{for} \quad k \in \mathbb{N}$$

To deduce the ordinary differential equations governing the evolution of the Fourier coefficients a_k, one has to evaluate the right-hand side of (1) at u_N given above, and then project the result onto the space X_N using $X^{1/2}$-orthogonal projections. Since the $\tilde{\varphi}_k$ are orthonormal in $X^{1/2}$, this amounts to determining the Fourier series representation of the right-hand side with respect to the $\tilde{\varphi}_k$, and then discarding the part of the series corresponding to Fourier modes greater than N. Inserting the expression (11) into the right-hand side of the Cahn–Hilliard equation we get with $\tilde{f}(u) := f(u) - f'(\mu)\, u$ the identity

$$\begin{aligned}(-\Delta(\varepsilon^2 \Delta u_N + f(u_N)), \tilde{\varphi}_k) &= (\varepsilon^2 \Delta u_N + f(u_N), -\Delta \tilde{\varphi}_k) \\ &= \kappa_k \cdot (\varepsilon^2 \Delta u_N + f'(\mu)\, u_N + \tilde{f}(u_N), \tilde{\varphi}_k) \\ &= \kappa_k (f'(\mu) - \varepsilon^2 \kappa_k) \cdot (u_N, \tilde{\varphi}_k) + \kappa_k \cdot (\tilde{f}(u_N), \tilde{\varphi}_k)\end{aligned}$$

for $k = 1, \ldots, N$, where $(\cdot, \cdot)$ denotes the standard $L^2(\Omega)$-scalar product. Together with the fact that $(u_N, \tilde{\varphi}_k) = a_k \cdot (\tilde{\varphi}_k, \tilde{\varphi}_k) = a_k/(1 + \kappa_k^2)$ one easily determines the ordinary differential equation for the coefficient a_k as

$$\dot{a}_k = \kappa_k (f'(\mu) - \varepsilon^2 \kappa_k) \cdot a_k + \kappa_k (1 + \kappa_k^2) \cdot \int_\Omega \tilde{f}(a_1 \tilde{\varphi}_1 + \cdots + a_N \tilde{\varphi}_N)\, \tilde{\varphi}_k \, dx \tag{12}$$

where $k = 1, \ldots, N$. For a fixed starting radius r, and exit radius R, we choose initial conditions uniformly in $(u_0 + X_N) \cap B_r(u_0)$ (uniform with respect to the Lebesgue measure on the finite-dimensional space X_N), and look at the probability distribution for the solutions of the above equation when they reach distance R from the equilibrium u_0. For sufficiently large N, the solutions of the system (12) will approximate the solutions of the Cahn–Hilliard equation (1) via (11). For more details we refer the reader to Bai *et al.*[2, 1] or Stuart.[24]

Before closing this subsection, let us add a few comments about our specific implementation for solving (12), where we consider the special case $\Omega = (0, 1)$, $\mu = 0$, and $f(u) = u - u^3$. Since we have to perform a large number of simulations in order to get reliable information on the exit distributions, a fast routine for evaluating the right-hand side of (12) is crucial. Obviously, the computationally most expensive part of determining the right-hand side is the calculation of the Fourier coefficients of the nonlinearity $\tilde{f}(u_N)$. This can be done efficiently using fast Fourier transforms. In fact, since we use the special nonlinearity $\tilde{f}(u) = -u^3$ for our simulations, our implementation actually provides a fast way for calculating the Fourier coefficients exactly. Finally, the ordinary differential equation (12) is solved using an embedded Runge–Kutta scheme with step size control.

2.2. Mode Distributions

In this and the following subsection, we present the results of our simulations. In order to get a good idea of how the Fourier modes $c_{k,R}(u_s)$ of the exit points $\mathscr{E}_R(u_s)$ are distributed, we perform 10,000 simulations each for two values of ε using various radii R. More specifically, we consider $\varepsilon = 0.04$ and $\varepsilon = 0.02$. In the first case, we choose 10,000 initial conditions u_s randomly in the ball $B_r(0) \cap X_N \subset X^{1/2}$ for $r = 0.03$ and $N = 20$. (Here and in the following, distances in $X^{1/2}$ are always measured with respect to the norm $\|\cdot\|_*$ defined above.) Then we compute the corresponding solutions of (1) and determine the exit points $\mathscr{E}_R(u_s)$ for $R = 1$, 5, 10, 30, and 60. In the case $\varepsilon = 0.02$ we choose $r = 0.01$, $N = 50$, and consider the exit radii $R = 1$, 10, 100, 200, and 500, again for 10,000 initial conditions u_s chosen uniformly in the ball $B_r(0) \cap X_N$.

In order to get some first information on the range of validity of the mathematical results by Grant and Maier-Paape, Wanner, we concentrate in this subsection on describing how mean value and standard deviation of the random variables $|c_{k,R}|$ develop as R increases. The reason for considering the absolute value $|c_{k,R}|$ instead of just $c_{k,R}$ is twofold. First, due to the symmetric setting that we use for our simulations, the mean value of $c_{k,R}$ is always 0. Also, since we would like to get information on the dominance of certain modes, considering the absolute value seems more appropriate.

These results are depicted in Figs. 4 and 5 for $\varepsilon = 0.04$ and $\varepsilon = 0.02$, respectively. In each subdiagram the horizontal axis represents the index k of the Fourier mode $c_{k,R}$. The solid polygon line shows the mean values of

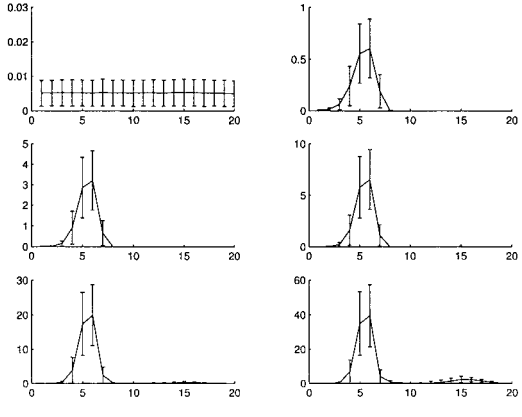

Fig. 4. Mode distribution parameters at different exit balls, $\varepsilon = 0.04$. The diagrams proceed left to right for growing radii R.

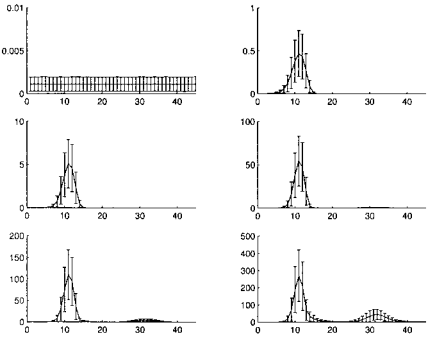

Fig. 5. Mode distribution parameters at different exit balls, $\varepsilon = 0.02$. The diagrams proceed left to right for growing radii R.

$|c_{k,R}|$, the vertical intervals indicate the corresponding standard deviations. The diagram in the upper left hand corner of each figure corresponds to the distribution of the initial conditions in $B_r(0) \cap X_N$, the following diagrams consider the exit distributions for increasing values of R as given above.

Looking at Figs. 4 and 5 one can immediately draw the following two conclusions. First of all, up to large radii R there is only a finite number of dominating modes, which actually seems to decrease with growing radius R. For $\varepsilon = 0.04$ these are modes 4 through 7, for $\varepsilon = 0.02$ modes 8 through 13 seem to dominate. All the remaining modes are close to 0 upon exiting the ball $B_R(0)$. Secondly, the standard deviations of the distribution of $|c_{k,R}|$ for the dominating modes is large, indicating a large range of probable values for $|c_{k,R}|$. Thus, our simulations show that for the initial condition ball radii r chosen above, one does not observe the result proved by Grant,[14] since it would imply extremely small standard deviations for all k. Rather, we obtain large standard deviations, indicating that the set of preferred exit points is higher-dimensional.

While the above observations were already conjectured by Maier-Paape and Wanner,[20,21] our simulations indicate that (1) exhibits other surprising behavior as well. Recall that in ref. 21 it was shown that for r and R proportional to $\varepsilon^{\dim \Omega}$ the subspace $\mathscr{Y}_\varepsilon$ generated by the dominating eigenfunctions determines the behavior of most solutions starting in $B_r(0)$ upon exit from $B_R(0)$. Our simulations indicate that this dominance can be observed up to considerably larger radii, namely $R \approx 30$ for $\varepsilon = 0.04$, and $R \approx 100$ for $\varepsilon = 0.02$. Note in particular that these values of R are increasing for decreasing ε. In addition, up to these unexpectedly large radii R, the temporal evolution of the Fourier coefficients resembles what one would expect from the linearized equation (3) in a striking way: The higher modes

converge to 0 exponentially fast, whereas the modes corresponding to positive eigenvalues $\tilde{\lambda}_{k,\varepsilon} > 0$ grow with exponential rate $\tilde{\lambda}_{k,\varepsilon}$.

At this point the reader might wonder why we claim that the size of the radii R is unexpected. To see this, consider a function $u \in X^{1/2}$, given by $u(x) = 6x^2 - 4x^3 - 1$. One can easily check that $\|u\|_* \approx 6.96$, well inside the ball of radius thirty in which we observe almost linear behavior. Now let $A_\varepsilon u := -\Delta(\varepsilon^2 \Delta u + u)$ as before, and define $F(u) := \Delta(u^3)$. Then the right-hand side of (1) is given by $A_\varepsilon u + F(u)$, with $A_\varepsilon u$ denoting the linear and $F(u)$ the nonlinear part. Furthermore, for $\varepsilon = 0.04$ we obtain

$$\|F(u)\|_{L^2(0,1)} \approx 2.47 \cdot \|A_\varepsilon u\|_{L^2(0,1)}, \qquad \|F(u)\|_* \approx 186.34 \cdot \|A_\varepsilon u\|_*.$$

In other words, even for values of $R = \|u\|_*$ which are considerably smaller than the values given in the last paragraph, one expects the nonlinear part $F(u)$ to dominate the linear behavior. Thus, one would not expect Figs. 4 and 5 to be as close to the linear case as they are.

To close this subsection, let us add some remarks about the onset of truly nonlinear behavior. According to Figs. 4 and 5 nonlinear behavior can be observed for large values of R in a specific way: In addition to the first bump of nontrivial eigenmodes, a secondary bump forms at higher modes. If k_0 denotes the mode lying in the center of the first bump, the secondary forms around mode $3k_0$. We think that this is a resonance effect due to the specific form of our cubic nonlinearity. Furthermore, we expect analogous behavior can be observed for two-dimensional domains Ω, in contrast to the numerical simulations of Copetti and Elliott.[7,8] Their spatial discretization may not have been fine enough to capture this phenomenon.

2.3. Density Estimates

The last subsection gives a first look at the distributions of the Fourier modes via estimating mean value and standard deviation of the variables $|c_{k,R}|$. Now we want to obtain more detailed information on the actual distributions. For some fixed values of k and R, we know that $c_{k,R} \in [-R, R]$. We want to get accurate information on the probability of $c_{k,R}$ being in an arbitrary subset $I \subset [-R, R]$. This information is coded in the associated *density function* $d_{k,R}: [-R, R] \to \mathbb{R}_0^+$ in the following way: For any measurable subset $I \subset [-R, R]$ the probability that the random variable $c_{k,R}$ takes values in I is given by the integral

$$\int_I d_{k,R}(x)\, dx$$

Thus, the density functions $d_{k,R}$ completely describe the exit distributions of the Fourier modes $c_{k,R}$.

There are many ways to obtain good estimates for the density functions of probability measures from Monte Carlo simulations, cf. for example Silverman[23] or Härdle.[15] We employ the *nonparametric kernel estimation technique*, which can be described as follows. Assume that our simulations produce n specific realizations Z_k, $k=1,...,n$, of the random variable $c_{k,R}$. Fix a *kernel function* K, i.e., a non-negative function $K\colon \mathbb{R}\to\mathbb{R}_0^+$ which is symmetric around 0 and satisfies $\int_{-\infty}^{\infty} K(t)\,dt=1$. Next, choose a positive *smoothing parameter* h, and define the rescaled kernels K_h by $K_h(x):=K(x/h)/h$, $x\in\mathbb{R}$. Then the *kernel density estimator* $\hat{d}_{k,R}$ for the unknown density $d_{k,R}$ is defined as

$$\hat{d}_{k,R}(x):=\frac{1}{n}\cdot\sum_{k=1}^{n}K_h(x-Z_k)=\frac{1}{nh}\cdot\sum_{k=1}^{n}K\left(\frac{x-Z_k}{h}\right)$$

In other words, the estimator $\hat{d}_{k,R}$ is obtained by centering a rescaled kernel K_h at each observation Z_k, and then averaging over these functions.

The choice of the kernel K is somewhat arbitrary, but some canonical choices can be found in Silverman[23] or Härdle.[15] For our simulations we choose the *triweight kernel* which is given by $K(t):=35/32\cdot(1-t^2)^3$ for $|t|\leqslant 1$, and $K(t)=0$ elsewhere. For this choice the density estimator $\hat{d}_{k,R}$ is always a C^2-function. Furthermore, choosing the "correct" smoothing parameter h is crucial. For extremely small h the estimate $\hat{d}_{k,R}$ will be noisy and show large fluctuations. On the other hand, for extremely large values of h one obtains a flat estimate $\hat{d}_{k,R}$ whose shape is roughly the shape of the kernel function, more or less independent of the data samples Z_k.

Our implementation of the above technique follows Härdle.[15] He describes the method of WARPing which significantly reduces the computational cost of the implementation. Furthermore, we use a suggestion due to Silverman[23] to take into account the bounded support and the symmetry of the distributions of the $c_{k,R}$. For more details we refer the reader to the above literature.

In Figs. 6 and 7 several density estimators are depicted. These are obtained from the simulations described in the last subsection. For $\varepsilon=0.04$ Fig. 6 contains estimators for the density functions $d_{k,R}$ for $R=1$ and $k=1,...,9$. Likewise, Fig. 7 shows estimators for $\varepsilon=0.02$, $R=1$, and $k=7,...,15$. In both cases the density functions are given by the solid lines. Furthermore, we choose the smoothing parameter $h=0.05$. According to these diagrams, we can roughly divide the modes into the following three categories:

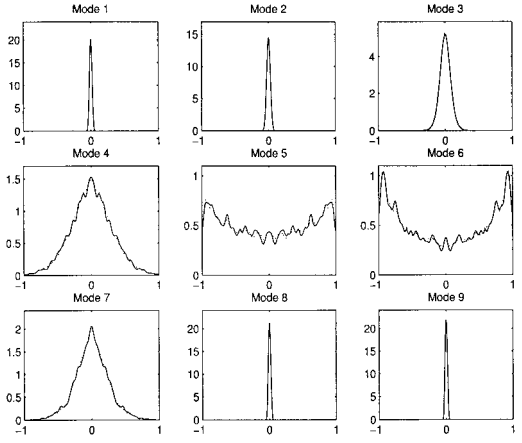

Fig. 6. Density functions of selected modes at $R = 1$, $\varepsilon = 0.04$. Solid lines correspond to the nonlinear Cahn–Hilliard equation, dotted lines to the linear.

• *Vanishing modes*: Upon exit from the ball $B_R(0)$, these modes vanish almost surely, i.e., the exit measure is a Dirac measure at 0. Thus, the density estimator is (almost) equal to the scaled kernel K_h. See modes 1, 2, 8, 9 in Fig. 6, as well as modes 7, 15 in Fig. 7.

• *Transitional modes*: These modes are likely to be close to zero, but exiting the ball $B_R(0)$ with a nonzero value definitely has positive probability. See modes 3, 4, 7 in Fig. 6, as well as modes 8, 9, 13, 14 in Fig. 7.

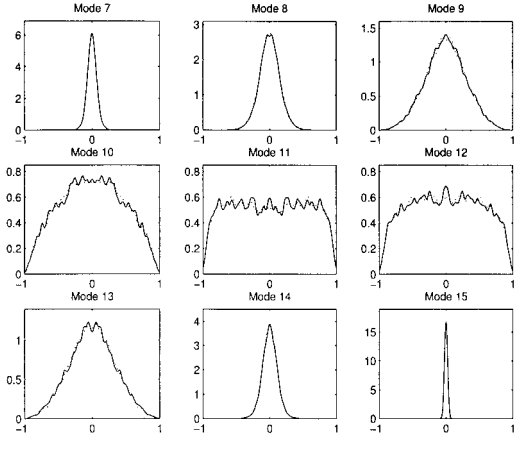

Fig. 7. Density functions of selected modes at $R = 1$, $\varepsilon = 0.02$. Solid lines correspond to the nonlinear Cahn–Hilliard equation, dotted lines to the linear.

• *Dominating modes*: When exiting the ball $B_R(0)$, these modes basically can take any value in the interval $[-R, R]$. See modes 5, 6 in Fig. 6, as well as modes 10, 11, 12 in Fig. 7.

Although we did not present the corresponding density estimators, the remaining modes all belong to the first category, i.e., they vanish almost surely. Moreover, the estimators obtained for larger values of R are similar to the ones depicted in Figs. 6 and 7—except the ones corresponding to modes in the secondary bump. However, since these are not important in our discussion, they are omitted.

Due to the inherent information loss through projection onto one-dimensional subspaces of $X^{1/2}$, the one-dimensional density functions from Figs. 6 and 7 can not give an accurate description of the geometry of the preferred exit set. Yet, they can provide some intuition. To that end, let us consider the uniform probability measure on the boundary S^{N-1} of the unit ball in $\mathbb{R}^N$. Projecting this measure to one of the coordinate axes furnishes a probability measure ν_N on $[-1, 1]$. It can easily be shown that this measure has a density function s_N given by

$$s_N(x) := c_N \cdot (1-x^2)^{(N-3)/2}, \qquad x \in (-1, 1)$$

with normalizing factor $c_N = \Gamma(N/2)/(\sqrt{\pi} \cdot \Gamma((N-1)/2))$.

Now consider the density estimators for modes 5 and 6 in Fig. 6. Both of these graphs resemble the graph of the function $s_2(x) = 1/(\pi \cdot \sqrt{1-x^2})$. This suggests that if we project the preferred exit set from $B_1(0)$ for $\varepsilon = 0.04$ onto the two-dimensional subspace of $X^{1/2}$ spanned by the 5th and 6th eigenmode, we would see something resembling the circle S^1. In fact, by estimating the density function for the distribution of the vector $(c_{5,1}(u_s), c_{6,1}(u_s)) \in \mathbb{R}^2$ from our simulations, this statement can be verified, i.e., the preferred exit set from $B_1(0) \subset X^{1/2}$ for $\varepsilon = 0.04$ is close to a one-dimensional closed curve. Similar considerations could be used to describe the preferred exit set for $\varepsilon = 0.02$ from our simulations, but we refrain from doing that.

Finally, let us come back to the discussion of the last subsection, where we conjecture that up to unexpectedly large radii R the solutions of the nonlinear Cahn–Hilliard equation (1) behave like the corresponding solutions of the linearized equation. Completely analogous to the simulations for (1), we also performed simulations for the linearized equation. The corresponding density estimators are depicted in Figs. 6 and 7 as dotted lines. The agreement of these estimators with the ones for the nonlinear equation is striking, and further backs our conjecture stated in the introduction.

3. UNEXPECTEDLY LINEAR BEHAVIOR

3.1. Validity of the Linear Regime

Although the simulations presented in the last section have been used to compare the mathematical explanations of spinodal decomposition due to Grant[14] and Maier-Paape, Wanner,[20,21] we learn something new. The simulations indicate that up to large radii R, the nonlinear Cahn–Hilliard equation seems to behave like its linearization, though as we argued by means of a simple example in Subsection 2.2 this is not at all what one would expect. Nonetheless, in this subsection we provide numerical evidence for the occurrence of this unexpectedly linear behavior, thus backing our Conjecture 1.1. Furthermore, we briefly describe the mechanism responsible for this. A rigorous mathematical explanation will be given in the forthcoming paper.[22]

As in the last section, we fix an initial radius r. Let $0 < p \ll 1$ be fixed; this will be interpreted as *maximal error tolerance*. Randomly pick an initial condition $u_s \in B_r(0) \cap X_N$, and compute the solutions u and v of equations (1) and (3) originating in u_s. For every $\varrho > r$, compute the first intersection points of u and v with $B_\varrho(0)$, and denote them by u_ϱ and v_ϱ, respectively. Finally, let R denote the first radius such that the *relative error* of u_R and v_R is equal to p, i.e., such that

$$\frac{\|u_R - v_R\|_*}{\|v_R\|_*} = p$$

In other words, we determine up to which radius R the orbits of (1) and (3) originating in u_s stay close to each other in a relative way.

The left diagram in Fig. 8 shows the results of 100 simulations of this type for each of five different ε-values. In each simulation we choose $r = 0.01$ (with respect to $\|\cdot\|_*$) and $p = 0.005$, and the diagram depicts the

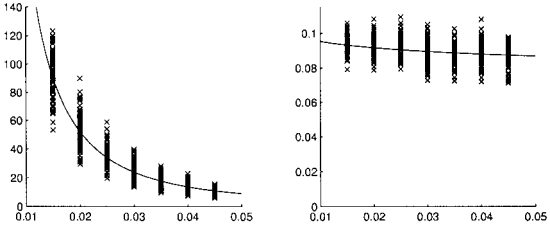

Fig. 8. Dependence of the maximal radius R on ε with respect to $\|\cdot\|_*$ (left) and the $L^\infty(0, 1)$-norm (right), relative error 0.5%.

obtained values of R plotted against ε. Thus, the radius up to which linear and nonlinear solutions differ by less than 0.5% grows as $\varepsilon \to 0$, and in fact is considerably larger than one would expect.

In order to deduce quantitative results about the nature of this growth, we use a least squares fit to estimate the parameters C_* and α_* in the polynomial function

$$R = C_* \cdot \varepsilon^{\alpha_*}$$

from the above data. These values are given by

$$C_* = 0.0287 \qquad \text{and} \qquad \alpha_* = -1.9182$$

and led to the formulation of Conjecture 1.1. Note that this asymptotic behavior of R does not contradict the fact that most orbits originating near $u_0 \equiv 0$ will approach profiles with values in the interval $[-1, 1]$. Rather, it indicates that the orbits develop high curvature terms, since those are of course incorporated in the norm $\|\cdot\|_*$.

Nonetheless, it is important to know the maximum norms of u_R and v_R, when their relative error is equal to 0.5%. For the above simulations, this information is shown in the right diagram of Fig. 8, where the maximum norm $\|u_R\|_{L^\infty(0,1)}$ is plotted against ε. This diagram indicates that as long as the maximum norm of u lies below a certain ε-independent threshold, the relative error of u and v is small. As before, we use a least squares fit to estimate the parameters C_∞ and α_∞ in

$$\|u_R\|_{L^\infty(0,1)} = C_\infty \cdot \varepsilon^{\alpha_\infty}$$

and this furnishes

$$C_\infty = 0.0731 \qquad \text{and} \qquad \alpha_\infty = -0.0580$$

In other words, the simulations shown in Fig. 8 indicate the validity of our Conjecture 1.1.

Yet, in view of the example given in Subsection 2.2 these results are surprising. In the remainder of this subsection we therefore describe the mechanism which is responsible for this unexpected behavior. Consider again the domain $\Omega = (0, 1)$, and let $W_k \subset X^{1/2}$ denote the one-dimensional subspace generated by the kth eigenfunction $\tilde{\varphi}_k$, or equivalently, by $\psi_k(x) = \sqrt{2} \cdot \cos k\pi x$. Let $A_\varepsilon u = -\Delta(\varepsilon^2 \Delta u + u)$ and $F(u) = \Delta(u^3)$ denote the linear and nonlinear parts of the right-hand side of the Cahn–Hilliard equation (1) for $f(u) = u - u^3$. For every $k \in \mathbb{N}$ and $u \in W_k$, we can

explicitly compute both $A_\varepsilon u$ and $F(u)$, and therefore also the $L^2(0, 1)$-norms of these functions. This yields

$$\frac{\|F(u)\|_{L^2(0,1)}}{\|A_\varepsilon u\|_{L^2(0,1)}} = \frac{3\sqrt{10}}{2} \cdot \frac{\|u\|_*^2}{(1+\kappa_k^2)\cdot|1-\varepsilon^2\kappa_k|} \tag{13}$$

for all $k \in \mathbb{N}$ and $u \in W_k$ with $A_\varepsilon u \neq 0$.

In order to get a first idea about the relative size of $F(u)$ versus $A_\varepsilon u$ we consider the one-dimensional subspaces W_k with $\tilde{\lambda}_{k,\varepsilon} \neq 0$ as test directions. Choose a small positive number $p > 0$. Then (13) implies for every $k \in \mathbb{N}$ such that $\tilde{\lambda}_{k,\varepsilon} \neq 0$, and every $u \in W_k \backslash \{0\}$ that

$$\frac{\|F(u)\|_{L^2(0,1)}}{\|A_\varepsilon u\|_{L^2(0,1)}} \leqslant p \quad \text{if and only if} \quad \|u\|_* \leqslant \frac{\sqrt{2p}}{\sqrt{3\sqrt{10}}} \cdot \sqrt{(1+\kappa_k^2)\cdot|1-\varepsilon^2\kappa_k|} \tag{14}$$

Thus, on the subspace W_1 the nonlinearity is considerably smaller than the linear part only as long as we have

$$\|u\|_* \leqslant 4.55 \cdot \sqrt{p} \cdot \sqrt{|1-\varepsilon^2\pi^2|}$$

Since the right-hand side of this inequality is of order ε^0 as $\varepsilon \to 0$, this again makes the result stated in Conjecture 1.1 appear surprising.

However, the situation is completely different if we consider subspaces W_k which are contained in the dominating subspace $\mathcal{Y}_\varepsilon$, spanned by the eigenfunctions corresponding to the largest eigenvalues. We define $\mathcal{Y}_\varepsilon$ as in refs. 20 and 21 to be the subspace spanned by eigenfunctions $\tilde{\varphi}_k$ such that the associated eigenvalues introduced in (6) satisfy $\tilde{\lambda}_{k,\varepsilon} \geqslant \gamma \cdot \lambda_\varepsilon^{\max}$, for some $0 < \gamma < 1$. Thus, the corresponding κ_k have the property

$$\frac{c_1}{\varepsilon^2} \leqslant \kappa_k \leqslant \frac{c_2}{\varepsilon^2}$$

for two constants $0 < c_1 < c_2 < 1$. Then (14) implies that on every $W_k \subset \mathcal{Y}_\varepsilon$ the nonlinear part $F(u)$ is considerably smaller than $A_\varepsilon u$ as long as

$$\|u\|_* \leqslant \frac{\sqrt{2p}}{\sqrt{3\sqrt{10}}} \cdot \sqrt{(c_1^2+\varepsilon^4)\cdot(1-c_2)} \cdot \varepsilon^{-2}$$

i.e., until $\|u\|_*$ reaches the order ε^{-2}, for $\varepsilon \to 0$.

The above calculations show that on certain subsets of the dominating space $\mathcal{Y}_\varepsilon$ the linear part $A_\varepsilon u$ dominates the nonlinear part $F(u)$ up to surprisingly large values of $\|u\|_*$. In fact, although this is not at all obvious,

it turns out that this statement remains valid on all of $\mathscr{Y}_\varepsilon$, and even in a suitable neighborhood of the dominating subspace. However, as indicated by the numerical results from the beginning of this subsection, the order of the admissible values of $\|u\|_*$ will be smaller than ε^{-2}, due to nonlinear superposition effects. See the forthcoming paper Sander, Wanner.[22]

We finally are in a position to describe the unexpectedly linear behavior. Due to Maier-Paape, Wanner,[20,21] most solutions of the Cahn–Hilliard equation (1) originating in a small neighborhood U_ε of the homogeneous equilibrium $u_0 \equiv \mu$ exit a larger neighborhood V_ε close to some dominating subspace $\mathscr{Y}_\varepsilon$. Furthermore, up to that point the behavior of the orbits is close to the linear behavior. But now the orbits enter a part of the phase space which is invariant with respect to the linearized equation (3), and where the nonlinear part is considerably smaller than the linear part. Thus, the solutions of the nonlinear equation (1) closely follow the linear orbits, until their norms exceed the threshold mentioned in Conjecture 1.1. In other words, the linearization drives most orbits into a part of phase space, where it can sustain its influence for much longer than normally possible. Sander, Wanner[22] contains the version of this conjecture which we are able to rigorously prove.

3.2. Eventually Linear Solutions

While the discussion of the last subsection explains why most solutions of (1) exhibit almost linear behavior for a long time, it also indicates that for certain initial conditions nonlinear behavior should set in much earlier. In this subsection we verify the existence of these exceptional initial conditions numerically. Moreover, we describe the evolution of these orbits.

Due to the discussion of the last subsection one expects that nonlinear behavior sets in early if an orbit of (1) is close to the subspace W_1 spanned by $\tilde{\varphi}_1$ or ψ_1. Figure 9 contains the results obtained from following the orbit u of the Cahn–Hilliard equation originating at $u_s = 0.01 \cdot \tilde{\varphi}_1$ for $\varepsilon = 0.02$. For this, we decompose the phase space $X^{1/2} = X^+ \oplus X^-$, where X^+ is a dominating subspace $\mathscr{Y}_\varepsilon$ generated by the eigenfunctions $\varphi_{k,\varepsilon}$ corresponding to eigenvalues $\lambda_{k,\varepsilon} \geqslant \frac{3}{4} \cdot \lambda_\varepsilon^{\max}$, and let X^- be generated by the remaining eigenfunctions. The solid line in the upper left diagram depicts the first part of the curve $\{(\|u^-(t)\|_*, \|u^+(t)\|_*): t \geqslant 0\}$ for the above orbit u, while the dotted line depicts the corresponding curve for the linear solution v of (3) originating in u_s. The two curves remain close to each other until $\|u(t)\|_*$ reaches the value 0.018, then they diverge. Thus, the nonlinear solution u remains close to the linear solution v only for a short time. This can also be seen in the lower left diagram, where the relative error $\|u-v\|_*/\|v\|_*$ is

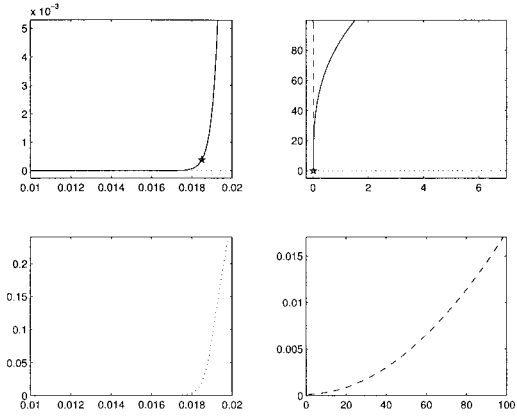

Fig. 9. Temporal evolution of the Cahn–Hilliard equation and its linearization starting at $u_s = 0.01 \cdot \tilde{\varphi}_1$ for $\varepsilon = 0.02$ in the $X^- - X^+$–coordinates (upper diagrams), and corresponding relative errors (lower diagrams).

plotted against the norm $\|u\|_*$. By the time $\|u\|_*$ reaches 0.02, the relative error is already bigger than 20%.

The behavior of the orbits u and v described in the last paragraph is what we expect. Nonetheless, the nonlinear orbit u exhibits linear behavior up to large radii as well. To see this, let $\bar{u}_s$ denote the point on the orbit of u satisfying the identity $\|\bar{u}_s\|_* = 0.0185$. This point is marked by a small star in the upper left diagram of Fig. 9. Moreover, let $\bar{v}$ denote the solution of (3) originating in $\bar{u}_s$. We claim that u and $\bar{v}$ remain close up to large radii, analogous to the last subsection. This is indicated in the upper right diagram of Fig. 9. Again, the solid line depicts part of the curve $\{(\|u^-(t)\|_*, \|u^+(t)\|_*): t \geqslant 0\}$ for u, the dotted line shows the corresponding curve for v, and the dashed line represents the new linear solution $\bar{v}$. Although the nonlinear solution visibly deviates from $\bar{v}$, the difference in X^--direction is relatively small if compared to the norm of u. This can also be seen in the lower right diagram, where the relative error $\|u - \bar{v}\|_* / \|\bar{v}\|_*$ is plotted against the norm $\|u\|_*$. Even when the norm $\|u\|_*$ reaches 80, the relative error is only 1%.

The above computations indicate that even for certain initial conditions which are not close to the dominating subspace $\mathscr{Y}_\varepsilon = X^+$, orbits exhibit linear behavior up to large radii. However, in this case an orbit u does not remain close to the linear solution v originating at the initial condition u_s. Rather, due to resonance effects caused by the nonlinearity, the orbit u quickly develops a nontrivial X^+-part, say for $u(\bar{t}) = \bar{u}_s$. Then u remains close to the linear solution starting at $\bar{u}_s$ for a long time. In other

words, the early onset of nonlinear behavior merely serves as a mechanism for selecting a different linear solution which then describes the behavior of the nonlinear orbit up to large radii. But once this selection has taken place, the effect of the nonlinearity dies out again.

We close this subsection with a remark on the probability for observing the different orbit behaviors. As mentioned at the end of Subsection 3.1, a combination of the results of Maier-Paape, Wanner[21] with the results in Sander, Wanner[22] will show that *most* orbits originating near the homogeneous equilibrium $u_0 \equiv \mu$ will remain close to the corresponding linear solution up to large radii. In this context, *most* has to be interpreted as *with probability close to* 1. Yet there is still a positive, albeit small, probability for observing different behavior, namely the one described in this subsection. Of course there are also solutions which do not fall into either of the above two categories. But we conjecture that the set of initial conditions near u_0 leading to solutions showing linear or eventually linear behavior in the above sense is prevalent, as defined in Hunt, Sauer, and Yorke.[17] This would explain why qualitatively, only one kind of behavior is observed inside the spinodal region.

4. CONCLUSIONS

We have performed extensive numerical simulations to gain better insight into the range of validity of existing mathematical explanations for spinodal decomposition. Besides testing the approaches due to Grant[14] and Maier-Paape, Wanner[20,21] we also discover new phenomena. Namely, the behavior of solutions of the Cahn–Hilliard equation (1) originating near the homogeneous equilibrium $u_0 \equiv \mu$ can be divided into three categories:

- *Unexpectedly linear behavior*: Solutions of (1) which start near a dominating subspace $\mathscr{Y}_\varepsilon$ as introduced in Maier-Paape, Wanner[20] will remain close to the corresponding linear solutions up to extremely large radii. A quantitative statement of this behavior based on our simulations is Conjecture 1.1.

- *Eventually linear behavior*: These are solutions which experience the influence of the nonlinearity in (1) already at small radii and therefore do not stay close to the corresponding linear solution. But caused by the nonlinear effect they quickly select a different linear solution and stay close to it up to large radii, similar to the first category.

- *Truly nonlinear behavior*: This category contains all the remaining solutions originating near $u_0 \equiv \mu$, such as certain unstable invariant manifolds tangent to non-dominating eigendirections.

In the forthcoming paper Sander, Wanner[22] we address solutions of the first category. We show that most solutions belong to this category. This, along with our conjecture that the first two kinds of solutions are prevalent, would imply that spinodal decomposition actually occurs "almost surely."

ACKNOWLEDGMENTS

We would like to thank Paul Fife, Stanislaus Maier-Paape, Leonard Sander, and Alastair Spence for useful discussions and comments. This work was done while we were at the Georgia Institute of Technology and the Universität Augsburg, Germany.

REFERENCES

1. F. Bai, C. M. Elliott, A. Gardiner, A. Spence, and A. M. Stuart, The viscous Cahn–Hilliard equation. Part I: Computations, *Nonlinearity* **8**:131–160 (1995).
2. F. Bai, A. Spence, and A. M. Stuart, Numerical computations of coarsening in the one-dimensional Cahn–Hilliard model of phase separation, *Physica D* **78**:155–165 (1994).
3. J. W. Cahn, Free energy of a nonuniform system. II. Thermodynamic basis, *J. Chem. Phys.* **30**:1121–1124 (1959).
4. J. W. Cahn, Phase separation by spinodal decomposition in isotropic systems, *J. Chem. Phys.* **42**:93–99 (1965).
5. J. W. Cahn, Spinodal decomposition, *Transactions of the Metallurgical Society of AIME* **242**:166–180 (1968).
6. J. W. Cahn and J. E. Hilliard, Free energy of a nonuniform system I. Interfacial free energy, *J. Chem. Phys.* **28**:258–267 (1958).
7. M. I. M. Copetti, *Numerical analysis of nonlinear equations arising in phase transition and thermoelasticity*, Ph.D. thesis (University of Sussex, 1991).
8. M. I. M. Copetti and C. M. Elliott, Kinetics of phase decomposition processes: Numerical solutions to Cahn–Hilliard equation, *Materials Science and Technology* **6**:273–283 (1990).
9. K. R. Elder and R. C. Desai, Role of nonlinearities in off-critical quenches as described by the Cahn–Hilliard model of phase separation, *Phys. Rev. B* **40**:243–254 (1989).
10. K. R. Elder, T. M. Rogers, and R. C. Desai, Early stages of spinodal decomposition for the Cahn–Hilliard–Cook model of phase separation, *Phys. Rev. B* **38**:4725–4739 (1988).
11. C. M. Elliott, The Cahn–Hilliard model for the kinetics of phase separation, in *Mathematical Models for Phase Change Problems*, J. F. Rodrigues, ed. (Birkhäuser, Basel, 1989), pp. 35–73.
12. C. M. Elliott and D. A. French, Numerical studies of the Cahn–Hilliard equation for phase separation, *IMA J. Appl. Math.* **38**:97–128 (1987).
13. P. C. Fife, Models for phase separation and their mathematics. Preprint, 1991.
14. C. P. Grant, Spinodal decomposition for the Cahn–Hilliard equation, *Communications in Partial Differential Equations* **18**:453–490 (1993).
15. W. Härdle, *Smoothing Techniques* (Springer-Verlag, New York/Berlin/Heidelberg, 1991).
16. J. E. Hilliard, Spinodal decomposition, in *Phase Transformations*, H. I. Aaronson, ed. (American Society for Metals, Metals Park, Ohio, 1970), pp. 497–560.

17. B. R. Hunt, T. Sauer, and J. A. Yorke, Prevalence: A translation-invariant "almost every" on infinite-dimensional spaces, *Bull. Amer. Math. Soc.* **27**:217–238 (1992).
18. J. M. Hyde, M. K. Miller, M. G. Hetherington, A. Cerezo, G. D. W. Smith, and C. M. Elliott, Spinodal decomposition in Fe-Cr alloys: Experimental study at the atomic level and comparison with computer models, *Acta metallurgica et materialia* **43**:3385–3426 (1995).
19. J. S. Langer, Theory of spinodal decomposition in alloys, *Ann. Phys.* **65**:53–86 (1971).
20. S. Maier-Paape and T. Wanner. Spinodal decomposition for the Cahn–Hilliard equation in higher dimensions. Part I: Probability and wavelength estimate, *Communications in Mathematical Physics* **195**(2):435–464 (1998).
21. S. Maier-Paape and T. Wanner, Spinodal decomposition for the Cahn–Hilliard equation in higher dimensions: Nonlinear dynamics, *Archive for Rational Mechanics and Analysis*, to appear.
22. E. Sander and T. Wanner, Unexpectedly linear behavior for the Cahn–Hilliard equation. Submitted for publication, 1999.
23. B. W. Silverman. *Density Estimation for Statistics and Data Analysis* (Chapman and Hall, London/New York, 1986).
24. A. Stuart, Perturbation theory for infinite dimensional dynamical systems, in *Theory and Numerics of Ordinary and Partial Differential Equations (Leicester, 1994)*, M. Ainsworth, J. Levesley, W. A. Light, and M. Marletta, eds. (Clarendon Press, 1995), pp. 181–290.